Journal of
Materials Chemistry A

Accepted Manuscript

This article can be cited before page numbers have been issued, to do this please use: X. Li, Z. Niu, J. Jiang and L. Ai, *J. Mater. Chem. A*, 2016, DOI: 10.1039/C6TA00223D.




ROYAL SOCIETY OF CHEMISTRY

www.rsc.org/materialsA

View Article Online
DOI: 10.1039/C6TA00223D

Journal Name

RSCPublishing

COMMUNICATION



# Cobalt nanoparticles embedded in porous N-rich carbon as an efficient bifunctional electrocatalyst for water splitting

Cite this: DOI: 10.1039/xoxxoooooox

Xingyue Li, Zhiguo Niu, Jing Jiang,* and Lunhong Ai*

Received ooth January 2012,
Accepted ooth January 2012

DOI: 10.1039/xoxxoooooox

www.rsc.org/

**Exploring efficient non-precious electrocatalysts with dual functionality working in same electrolyte towards for both the hydrogen evolution reaction (HER) and oxygen evolution reaction (OER) is crucial to develop various devices for conversion, storage and usage of renewable energy. In this communication, we report a novel bifunctional electrocatalyst based on cobalt nanoparticles (NPs) embedded in the porous N-rich carbon (PNC/Co) derived from a cobalt-containing metal-organic framework, which can serve as both the active cathode and anode materials to drive the overall water splitting in alkaline media for simultaneous electro-generation of hydrogen and oxygen gases. In 1.0 M KOH electrolyte, the PNC/Co achieves small overpotentials at a current density of 10 mA cm$^{-2}$ and yields high Faradaic efficiency towards both the HER and OER. When fabricated as the alkaline water electrolyzer, the bifunctional PNC/Co affords 10 mA cm$^{-2}$ at a cell voltage of 1.64 V.**

Owing to the depletion of limited fossil fuels and their excessive consumption associated severe environmental problem, it is becoming a challenging task of scientific community to search for affordable sustainable alternative energy from renewable resources. Hydrogen ($H_2$) appears to be a renewable and environment-friendly energy sources and is considered as a principal energy carrier for the future,[1, 2] which can be potentially and ideally produced from the electro- or photochemical dissociation of water. Such process offers the simplest and economically viable approach to the efficient conversion and storage of intermittent energy sources (e.g. wind and solar) into potentially inexhaustible fuel sources. In general, the overall reaction of water splitting ($2H_2O \rightarrow 2H_2 + O_2$, $\Delta E$=-1.23 V) consists of both reduction (hydrogen evolution reaction (HER): $2H^+ + 2e^- \rightarrow H_2$, $E^0$=0.00 V vs RHE) and oxidation (oxygen evolution reaction (OER): $2H_2O \rightarrow 4H^+ + O_2 + 4e^-$, $E^0$ = 1.23 V vs RHE) half-reactions. However, both the HER and OER are intrinsically efficiency-limited,[3, 4] which require the efficient electrocatalysts to accelerate the reaction rate and further to reduce the energy consumption. Although the Pt-group metals and Ru- or Ir-based compounds are considered as the most active catalysts for the HER and OER, respectively, the scarcity and high cost unfortunately hinder their large-scale commercial applications. Thus, it is highly demanded to explore active but stable non-precious alternative catalysts based on earth-abundant elements for water splitting.

Furthermore, developing a new type of bifunctional materials performed as both the HER and OER catalyst has become a significant concern about the sustainable overall water splitting. To drive both reactions for simultaneous generation of hydrogen and oxygen gases, such same one catalyst with dual functionality should work in the same electrolyte (strongly acidic or basic electrolyte) to minimize the overpotentials.[5] However, this requirement is a big challenge for the earth-abundant catalysts because good catalysts in acidic electrolyte often tend to be inactive or even unstable in basic electrolyte and vice versa. For example, the most studied $MoS_2$ is an active catalyst for HER in acidic electrolyte, which is unstable in alkaline media.[6] Similarly, the OER-active metal oxides and (oxy)hydroxides are also unstable in acidic media. So far, very limited example has been established to exploring bifunctional catalysts for overall water splitting, mainly including some cobalt-, nickel- and iron-based catalysts, such as iron phosphide,[7, 8] $Ni_2P$,[9] $Ni_4P_5$,[10] Co-P,[11] NiSe,[12] NiFe-LDH,[13] $NiFeO_x$,[14] CoSe,[15] $NiCo_2S_4$,[16] NiMo alloy,[17] porous Co phosphide/phosphate thin film (PCPTF),[18] and cobalt-cobalt oxide/N-doped carbon hybrids ($CoO_x$@CN).[19] Undoubtedly, it is highly desirable to develop efficient bifunctional catalysts with both the HER and OER performances in the same electrolyte, which would be crucial for simplifying the apparatus and lowering the manufacturing cost.

Herein, we exploit the unique composition and structure of Co-based zeolitic imidazolate framework (ZIF-67) as a precursor to synthesize the cobalt nanoparticles (NPs) embedded in porous N-rich carbon (PNC/Co). The resulting PNC/Co performs as a bifunctional catalyst that has high activity towards both the HER and OER in strongly alkaline media. In 1.0 M KOH electrolyte, the PNC/Co achieves small overpotentials at a current density of 10 mA cm$^{-2}$ and yields high Faradaic efficiency towards both the HER and OER. When fabricated as the alkaline water electrolyzer, the bifunctional PNC/Co affords a water-splitting current of 10 mA cm$^{-2}$ at a cell voltage of 1.64 V.

Figs. 1a and 1b show the scanning electron microscopy (SEM) images of ZIF-67 crystals before carbonization. It reveals that the as-

synthesized ZIF-67 crystals possess a regular rhombic dodecahedral morphology composed of well-defined rhombus faces and straight edges. The average size of the ZIF-67 is about 1.5 μm. In the X-ray diffraction (XRD) pattern (Fig. S1a, ESI†), all the diffraction peaks match well with the simulated pattern, indicating the formation of ZIF-67 framework. The strong and sharp profiles further confirm the high crystallinity of the synthesized ZIF-67 crystal. After the pyrolysis treatment, the carbonized products substantially retain the original morphology of the ZIF-67 crystal. However, the smooth surfaces of the precursor became rough and concave and its size appeared remarkable shrinkage (Figs. 1c and 1d). This could be associated with the massive loss of organic components during the annealing process. The energy dispersive X-ray spectroscopy (EDS) of the PNC/Co (Fig. S2, ESI†) reveals the coexistence of C, N, O and Co with a mass fraction of 45.14%, 4.38%, 17.23% and 33.25%, respectively. The presence of oxygen species could be resulted from superficial oxidation of cobalt in air. The corresponding SEM-EDS elemental mapping reveals the homogenous distribution of these elements species (Fig. 1e) in the PNC/Co. The transmission electron microscopy (TEM) images of the annealed products (Fig. 2b) further demonstrate that the PNC/Co maintains the pristine rhombic dodecahedron (Fig. 2a). Some PNC/Co presents loose structure (Fig. 2c), possibly because of a relatively large structural strain in rhombic dodecahedron during the thermal decomposition process. It is clear that the Co NPs (black dots) with the average sizes of about 10 nm are well embedded and uniformly dispersed in the porous rhombic dodecahedron carbon framework (grey matrix) without obvious aggregation (Fig. 2d and Fig. 2e). Interestingly, a number of flexible carbon nanotubes (CNTs) with a diameter of ~14 nm extended from the surface of carbon framework could be clearly observed (Fig. 2c and Fig. 2e). The corresponding HRTEM images (Fig. 2f) reveal the distinct lattice fringes with a spacing of 0.20 nm for (111) plane of the highly crystalline Co NPs which are wrapped in the continuous graphitic carbon layers.

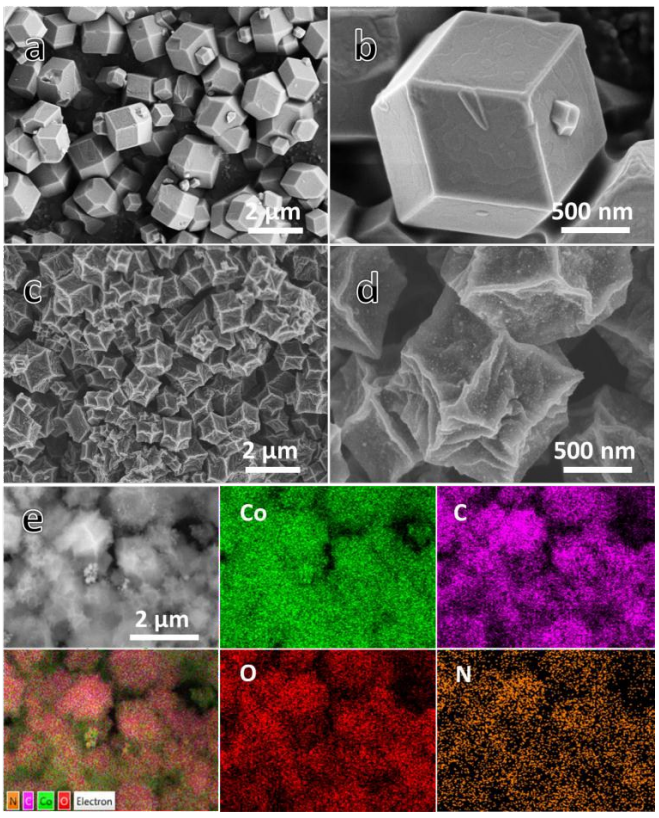


**Fig. 1** SEM images of the ZIF-67 (a,b) and PNC/Co (c,d). SEM-EDS elemental mapping images (e) of the PNC/Co.

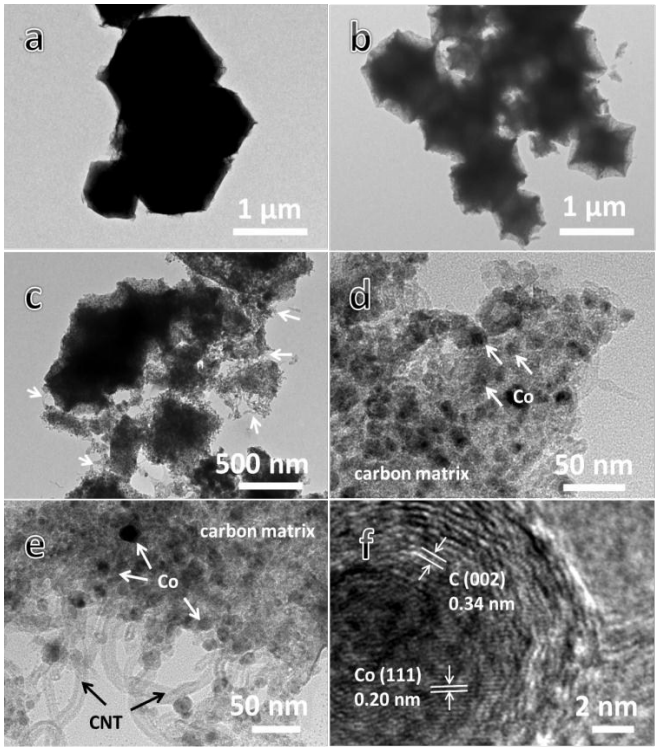


**Fig. 2** TEM images of the ZIF-67 (a) and PNC/Co (b-e), HRTEM image (f) of the PNC/Co.

In addition to the morphology evolution, the change in crystallographic structure after the pyrolysis process was also confirmed by the XRD patterns (Fig. S1b, ESI†). Compared with the strong peaks of the ZIF-67 precursor, the PNC/Co product exhibits the relatively broad peaks. The main peaks match well with the fcc structured metallic Co (JPCDS file no. 15-0806), along with a broad peak at approximately 25 ° belonging to the (002) interlayer peak of graphitic carbon. This result suggests complete transition of the ZIF-67 to the PNC/Co.

X-ray photoelectron spectroscopy (XPS) was conducted to further determine the chemical composition and valence state of the PNC/Co. Survey spectra in Fig. S3a shows that the product consists of the carbon, nitrogen, cobalt and oxygen elements. The high resolution C 1s spectrum (Fig. S3b, ESI†) suggests the presence of C=C-C (284.6 eV) and C-N (285.5 eV) in the PNC/Co. The high-resolution N 1s spectrum (Fig. S3c, ESI†) can be well-fitted into four peaks at 398.3, 399.0, 400.3, and 401.6 eV, corresponding to the pyridinic-N, Co-$N_x$, pyrrolic-N, and graphitic-N, respectively.[20] Deconvolution of the Co 2p spectrum (Fig. S3d, ESI†) reveals the presence of metallic $Co^0$ (778.0 eV) and oxidized Co species ($Co^{3+}$: 780.5 eV and $Co^{2+}$: 782.4 eV)[19, 21] due to the surface oxidization of metallic Co in the PNC/Co in air. The temperature programmed reduction ($H_2$-TPR) further confirms the presence of oxidized Co species in the PNC/Co[22] and supports above XPS results (Fig. S10d, ESI†).

The porosity of the PNC/Co was determined by $N_2$ adsorption-desorption isotherms (Fig. S4a, ESI†). The PNC/Co displays an intermediate mode between type I and type IV isotherms with the steep $N_2$ uptakes at low relative pressure and the distinct hysteresis loops at a relative pressure range from 0.40 to 1.0, indicating the presence of micro-/mesoporous structures. Such hierarchically

View Article Online
DOI: 10.1039/C6TA00223D
COMMUNICATION



micro/mesoporous structures were also reflected by the pore size distributions (Fig. S4b, ESI†). The Brunauer-Emmett-Teller (BET) surface area of the PNC/Co is calculated to be 91 $m^2 g^{-1}$. Although these BET values were much lower than that of the ZIF-67 precursor (> 1500 $m^2 g^{-1}$),[23] the PNC/Co still hold relatively high surface area for electrocatalysis applications.

The electrocatalytic OER performance of the PNC/Co was first tested by using a typical three-electrode cell setup in 1.0 M KOH solution. Fig. S5 shows the typical cyclic voltametry (CV) of the PNC/Co in 1.0 M KOH solution at a scan rate of 100 mV $s^{-1}$. Clearly, the PNC/Co experienced a preoxidation process with a prominent anodic peak prior to the onset of OER, which could be ascribed to the oxidation of metallic Co in the PNC/Co to higher valent states. Such initial activation phenomenon is similar to the cases for previously reported metallic Co NPs,[24] Co−P films[11], CoP NPs[25] and $Co_4N$ nanowires.[26] Fig. 3a shows the anodic polarization curves obtained from linear sweep voltammetry (LSV) at a scan rate of 5 mV $s^{-1}$ for the PNC/Co, which were deposited on the glassy carbon electrode (GCE) with a mass loading of ~0.35 mg $cm^{-2}$. The ZIF-67 and commercial $RuO_2$ catalyst were also measured using the similar approach as a comparison. The $RuO_2$ catalyst exhibits the expected OER activity with a large current density at a low overpotential. The ZIF-67 is also capable for electrocatalyzing oxygen evolution, but its relatively low OER activity yields a high onset potential (~1.71 V versus the RHE) and a low anodic current in the measured potential widow. The PNC/Co displays the much higher OER activity than that of the ZIF-67, as the significantly larger anodic current at the same overpotential is produced by the PNC/Co. More specifically, driving a current density of 10 mA $cm^{-2}$ (the current density expected from a 12.3% efficient solar water splitting device), the PNC/Co only demands an overpotential of ~370 mV. The electrocatalytic OER kinetics of the PNC/Co was also characterized by the Tafel slope, which can be obtained from the linear region of the Tafel by fitting the experimental data to the Tafel equation ($\eta = b \log j + a$, where $\eta$ is overpotential, $j$ is the current density, and $b$ is the Tafel slope). As shown in Fig. 3b, the Tafel slope of 48 mV $dec^{-1}$ for the $RuO_2$ catalyst agrees with the reported value. The Tafel slopes of the PNC/Co and ZIF-67 are 76 and 79 mV $dec^{-1}$, respectively, suggesting the obviously similar kinetics of the OER activity between the two catalysts. We further determined the stability of the PNC/Co for OER catalysis under such strongly alkaline condition. As shown in Fig. 3c, after 1000 cycles, the PNC/Co still performs as good as the initial cycle. The chronopotentiometry test also confirms the long-term stability of the PNC/Co, which can retain its catalytic activity after chronopotentiometric electrolysis of 10 h (Fig. 3d). Of note, during the first 2000 s of the electrolysis, the required potential gradually increases, which could be originated from the oxidation of uncovered or less-covered Co NPs in the PNC/Co to transform it to the OER active state. This result is consistent with the recent observation on the $Ni_2P$/Ni/nickel foam.[27] Whereas, the potential for electrolysis increases after 16000 s, which may be ascribed to the oxidation of the PNC-wrapped Co NPs. As the OER proceeds, the interior Co NPs are completely oxidized and the potential for electrolysis is back to the initial data. After the OER stability tests, we performed SEM, HRTEM, XRD and XPS characterizations to understand the OER performance of the PNC/Co. SEM and TEM observations (Fig. S6, ESI†) results indicate that the PNC/Co basically preserves original profiles after cycling test in alkaline condition. However, HRTEM observations demonstrate the gradual amorphization of Co NPs in the PNC/Co (Fig. S7, ESI†). Correspondingly, the crystalline structure of the PNC/Co has an obvious change after cycling tests. XRD data reveals that the crystallinity of the Co NPs becomes very poor (Fig. S8a, ESI†) after OER catalysis. In fact, the PNC/Co catalysts are prone to corrosion after immersed in 1.0 M KOH for one day (Fig. S9, ESI†), because it is not fully protected but partially covered by the PNC/Co. In addition, the XPS results indicate the gradual oxidation of Co NPs in the PNC/Co and nearly complete oxidation into $Co^{3+}$ species after 1000th potential cycling (Fig. S8b, ESI†). These results confirm that Co NPs are not the real active catalyst for OER but the in situ formed oxidized Co species from entrapped Co would be OER active sites, which are consistent with previously reported metallic Co for OER catalysis[28] and agree well with the recent observations on other Co-based OER catalysts.[11, 25, 26, 29] We further carried out the contrast experiments to reveal the role of the surface oxidized Co for OER catalysis. The reduced PNC/Co can be obtained by chemical reduction of the PNC/Co during $H_2$-TPR test. After hydrogen reduction, accompanying with a decrease in amount of oxidized Co, the PNC/Co exhibits the decreased activity for OER catalysis (Fig. S10e, ESI†). Similarly, creating suitable amounts of oxidized Co in the PNC/Co is favorable for promoting its OER performance (Fig. S10b, ESI†). These results reveal that the oxidized Co would be also the OER active sites. To further understand the OER performance of the PNC/Co, the bare PNC were prepared by extensively washing it with HF solution (10 wt %) to remove the deposited Co species. Of note, only PNC without Co NPs exhibits negligible catalytic current toward OER, which is consistent with the previous works on nitrogen-doped carbon materials,[30] confirming both the oxidized Co and in situ formed oxidized Co from entrapped Co contribute to the observed OER performance of the PNC/Co.

Moreover, the obvious oxygen bubbles quickly generate on the PNC/Co modified on GCE during the chronopotentiometry measurements, suggesting the high efficiency of the PNC/Co (Fig. S11, ESI†). Considering that bubbles will hinder the contact between electrode and electrolyte, we remove the bubbles generated in the OER process by stirring. The Faradaic efficiency of the PNC/Co was measured from bulk electrolysis in 1.0 M KOH solution in a gas-tight H-type electrochemical cell. The amount of generated oxygen in the experiment matches well with the theoretical amount of oxygen under the total charge during the electrolysis process (Fig. S12, ESI†), suggesting the Faradaic efficiency is close to 96%.

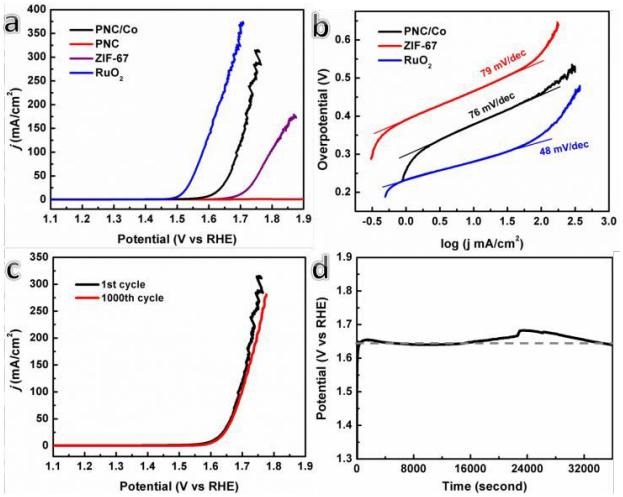


**Fig. 3** (a) Anodic polarization curves of the PNC/Co, ZIF-67, PNC and commercial $RuO_2$ catalysts with a scan rate of 5 mV $s^{-1}$ in 1.0 M KOH solution. (b) Tafel plots of the PNC/Co, ZIF-67, and commercial $RuO_2$ catalysts. (c) Durability test for the PNC/Co by CV scanning at 1000th cycles in 1.0 M KOH solution. (d) Chronopotentiometric durability test of the PNC/Co at a constant current density of ~10 mA $cm^{-2}$.

The electrocatalytic HER activity of the PNC/Co was also examined in three-electrode system in such strongly alkaline media. Fig. 4a shows the cathodic polarization curves of the PNC/Co at a scan rate of 5 mV $s^{-1}$ in 1.0 M KOH solution. The control experiments were conducted using the ZIF-67, PNC and commercial Pt/C catalyst as references. In 1.0 M KOH solution, the Pt/C exhibits the best HER activity, whereas the ZIF-67 present the poor activity for catalyzing HER. Also, the bare PNC exhibits the similar poor activity to the ZIF-67, which is consistent with the previous works on nitrogen-doped carbon materials.[19, 31, 32] The PNC/Co exhibits a remarkably high activity with an onset potential of ~270 mV. To achieve a HER current density of 10 mA $cm^{-2}$, an overpotantial of as small as 298 mV is needed. Of note, the LSV curves of the PNC/Co by using Pt wire and graphite rod as the counter electrode almost overlap (Fig. S13, ESI†), indicating the intrinsic HER activity of the PNC/Co catalyst instead of Pt contamination.[33] The Tafel curve (Fig. 4b) of the PNC/Co shows a slope of 131 mV/dec, which is much lower than that of the ZIF-67 (254 mV/dec) and PNC (159 mV/dec). The stability of the PNC/Co for the electrocatalytic HER in such a strongly alkaline environment was further evaluated. After 1000 cycles of continuous operation, the polarization curve maintains a similar shape to the initial one (Fig. 4c). Also, the operational overpotential is almost retained during 10 h electrochemical running at current density of 10 mA $cm^{-2}$ (Fig. 4d). SEM and TEM images show that the post-OER catalysts maintain the original configuration of the PNC/Co (Fig. S14, ESI†). It should be noted that the potential gradually decreases during chronopotentiometric electrolysis, which could be attributed to the gradual reduction of $Co^{3+}$ in the oxidized Co in the PNC/Co. Correspondingly, XPS results of the post-HER catalysts indicate the partial reduction of the oxidized Co in the PNC/Co (Fig. S15b, ESI†), as more amounts of $Co^{2+}$ species appear in the PNC/Co after HER. XRD (Fig. S15a, ESI†) and HRTEM (Fig. S16, ESI†) analysis reveal that in situ corrosion and amorphization are also accompanied with HER catalysis. Interestingly, the reduced PNC/Co exhibits the increased activity for HER catalysis (Fig. S10f, ESI†). Whereas, increasing amounts of oxidized Co in the PNC/Co has the negatively effect on the HER (Fig. S10c, ESI†). These results confirm the metallic Co in the PNC/Co would be active sites for HER catalysis, different from its OER catalysis. Since metal-centered catalytic sites are widely known to be deactivated by the $SCN^-$ in acidic[34, 35] and alkaline[36, 37] conditions. The addition of $SCN^-$ (5 mM) into the electrolyte greatly inhibits the HER activity of the PNC/Co (Fig. S17, ESI†), suggesting that a certain amount of metallic cobalt sites are deactivated by the $SCN^-$ ions, which supports metallic Co in the PNC/Co represents the HER active center. In addition, we also test the Faradaic efficiency of the PNC/Co for hydrogen evolution, which is determined to be nearly 100% (Fig. S18, ESI†).

Inspired by above results that the PNC/Co can work as both OER and HER electrocatalyst, we further design and construct a two-electrode cell using PNC/Co deposited onto a nickel foam (1 mg $cm^{-2}$) as both anode and cathode to extend this system towards practical electrolysis applications. As shown in Fig. S19, our electrolyzer can afford 10 mA $cm^2$ at a cell voltage of ~1.64 V in 1.0 M KOH. This voltage compares favourably to that of the previously reported bifunctional electrocatalysts for overall water splitting in alkaline media (Table S1, ESI†).

On the basis of above structural characteristics and intrinsic properties of the PNC/Co, we infer that the PNC/Co offers several advantages for electrocatalytic water splitting. First, choosing ZIF-67 as both the carbon and metal sources to prepare ultrasmall-sized Co particles embedded in carbon skeleton prevents Co NPs from aggregation and thus provides more exposed Co active sites. The carbon framework not only provides a good supporting matrix to maintain the structural integrity by mitigating the mechanical strain, but also enables the reduction of the particle-to-particle interfacial resistance by preventing particle aggregation. Second, the measurement on electrochemical surface area shows that the PNC/Co exhibits a relatively larger double-layer capacitance of 40.8 mF $cm^{-2}$ (Fig. S20, ESI†), which is markedly higher than or comparable with reported Co-based electrocatalysts, such as metallic $CoS_2$,[38] $CoSe_2$,[39] and $CoO_x$@CN.[19] This suggests a large effective electrochemical surface area (ECSA) of the PNC/Co, which is consistent with its large BET specific surface area of 91 $m^2$ $g^{-1}$. In addition, the well-developed porosity in the PNC/Co allows the easy diffusion of electrolytes into the carbon framework, enabling an effective channel for their fast transportation and efficient transfer of reactants to the catalyst's active sites, further promoting the performance for electrochemical water splitting. Third, the synergistic cooperation of in situ formed oxidized Co and metallic Co plays a significant role in enhancing the OER activity, similar to that of the recently reported $Co/Co_3O_4$.[40] The underneath metallic Co acts as a current reservoir to provide an effective electron pathway to the outer amorphous oxidized Co.

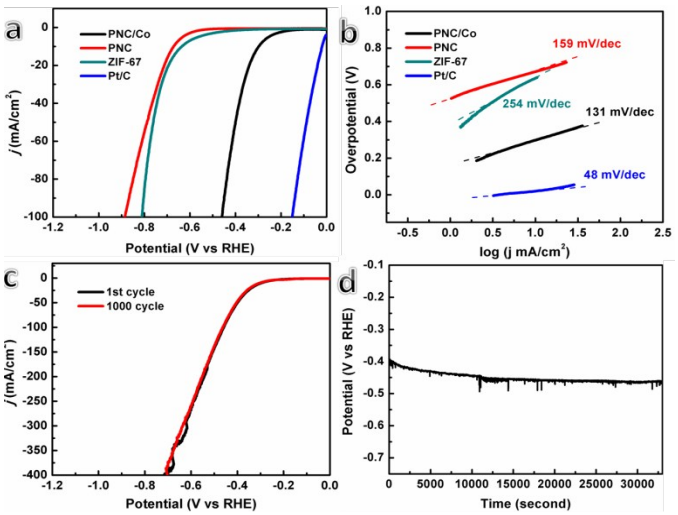


**Fig. 4** (a) Cathodic polarization curves of the PNC/Co, ZIF-67, PNC and commercial Pt/C catalysts with a scan rate of 5 mV $s^{-1}$ in 1.0 M KOH solution. (b) Tafel plots of the PNC/Co, ZIF-67, PNC, and commercial Pt/C catalysts. (c) Durability test for the PNC/Co by CV scanning at 1000th cycles in 1.0 M KOH solution. (d) Chronopotentiometric durability test of the PNC/Co at a constant current density of ~10 mA $cm^{-2}$.

In summary, we have demonstrated the MOF-derived PNC/Co can serve as an efficient bifunctional catalyst to drive the overall water splitting in alkaline media for simultaneous electro-generation of hydrogen and oxygen gases. To catalyze both the HER and OER in two-electrode cell for overall water splitting, the PNC/Co achieves 10 mA $cm^{-2}$ at a cell voltage of 1.64 V. These findings highlight the potential of the PNC/Co as both the cathode and anode electrocatalysts for designing a cost-effective electrochemical water splitting devices for clean energy utilization.

## Acknowledgements

View Article Online
DOI: 10.1039/C6TA00223D
COMMUNICATION



This work was supported by the National Natural Science Foundation of China (51572227, 21207108), the Sichuan Youth Science and Technology Foundation (2013JQ0012), and the Research Foundation of CWNU (14E016).

## Notes and references

Chemical Synthesis and Pollution Control Key Laboratory of Sichuan Province, College of Chemistry and Chemical Engineering, China West Normal University, 1 Shida Road, Nanchong 637002, P.R. China. E-mail: 0826zjjh@163.com; ah_aihong@163.com; Tel/Fax: +86-817-2568081

Electronic Supplementary Information (ESI) available: [details of any supplementary information available should be included here]. See DOI: 10.1039/c000000x/

1. H. B. Gray, *Nat. Chem.*, 2009, **1**, 7.
2. N. S. Lewis and D. G. Nocera, *Proc. Natl. Acad. Sci. U. S. A.*, 2006, **103**, 15729-15735.
3. R. D. L. Smith, M. S. Prevot, R. D. Fagan, Z. Zhang, P. A. Sedach, M. K. J. Siu, S. Trudel and C. P. Berlinguette, *Science*, 2013, **340**, 60-63.
4. M. G. Walter, E. L. Warren, J. R. McKone, S.W. Boettcher, Q. Mi, E. A. Santori and N. S. Lewis, *Chem. Rev.*, 2010, **110**, 6446-6473.
5. E. A. Hernandez-Pagan, N. M. Vargas-Barbosa, T. Wang, Y. Zhao, E. S. Smotkin and T. E. Mallouk, *Energy Environ. Sci.*, 2012, **5**, 7582-7589.
6. D. Merki, S. Fierro, H. Vrubel and X. Hu, *Chem. Sci.* , 2011, **2**, 1262-1267.
7. Y. Yan, B. Y. Xia, X. Ge, Z. Liu, A. Fisher and X. Wang, *Chem. Eur. J.*, 2015, **21**, 18062-18067.
8. Y. Yan, L. Thia, B. Y. Xia, X. Ge, Z. Liu, A. Fisher and X. Wang, *Adv. Sci.*, 2015, **2**, DOI: 10.1002/advs.201500120.
9. L.-A. Stern, L. Feng, F. Song and X. Hu, *Energy Environ. Sci.*, 2015, **8**, 2347-2351.
10. M. Ledendecker, S. K. Calderón, C. Papp, H.-P. Steinrück, M. Antonietti and M. Shalom, *Angew. Chem. Int. Ed.*, 2015, **54**, 12361-12365.
11. N. Jiang, B. You, M. Sheng and Y. Sun, *Angew. Chem. Int. Ed.*, 2015, **54**, 6251-6254.
12. C. Tang, N. Cheng, Z. Pu, W. Xing and X. Sun, *Angew. Chem. Int. Ed.*, 2015, **54**, 9351-9356.
13. J. Luo, J.-H. Im, M. T. Mayer, M. Schreier, M. K. Nazeeruddin, N. G. Park, S. D. Tilley, H. Fan and M. Gratzel, *Science*, 2014, **345**, 1593-1596.
14. H. Wang, H.-W. Lee, Y. Deng, Z. Lu, P.-C. Hsu, Y. Liu, D. Lin and Y. Cui, *Nat. Coummun.*, 2015, **6**, 7261.
15. T. Liu, Q. Liu, A. M. Asiri, Y. Luo and X. Sun, *Chem. Commun.*, 2015, **51**, 16683-16686.
16. D. Liu, Q. Lu, Y. Luo, X. Sun and A. M. Asiri, *Nanoscale*, 2015, **7**, 15122-15126.
17. J. Tian, N. Cheng, Q. Liu, X. Sun, Y. He and A. M. Asiri, *J. Mater. Chem. A*, 2015, **3**, 20056-20059.
18. Y. Yang, H. Fei, G. Ruan and J. M. Tour, *Adv. Mater.*, 2015, **27**, 3175-3180.
19. H. Jin, J. Wang, D. Su, Z. Wei, Z. Pang and Y. Wang, *J. Am. Chem. Soc.*, 2015, **137**, 2688-2694.
20. Z. Zhang, J. Hao, W. Yang and J. Tang, *ChemCatChem*, 2015, **7**, 1920-1925.
21. J. Jiang, A. Zhang, L. Li and L. Ai, *J. Power Sources*, 2015, **278**, 445-451.
22. Y. Ji, Z. Zhao, A. Duan, G. Jiang and J. Liu, *J. Phys. Chem. C*, 2009, **113**, 7186-7199.
23. X. Li, X. Gao, L. Ai and J. Jiang, *Chem. Eng. J.*, 2015, **274**, 238-246.
24. L. Wu, Q. Li, C. H. Wu, H. Zhu, A. Mendoza-Garcia, B. Shen, J. Guo and S. Sun, *J. Am. Chem. Soc.*, 2015, **137**, 7071-7074.
25. J. Ryu, N. Jung, J. H. Jang, H.-J. Kim and S. J. Yoo, *ACS Catal.*, 2015, **5**, 4066-4074.
26. P. Chen, K. Xu, Z. Fang, Y. Tong, J. Wu, X. Lu, X. Peng, H. Ding, C. Wu and Y. Xie, *Angew. Chem. Int. Ed.*, 2015, **54**, 14710-14714.
27. B. You, N. Jiang, M. Sheng, M. W. Bhushan and Y. Sun, *ACS Catal.*, 2016, **6**, 714-721.
28. N. H. Chou, P. N. Ross, A. T. Bell and T. D. Tilley, *ChemSusChem*, 2011, **4**, 1566-1569.
29. X. Liu, J. Jiang and L. Ai, *J. Mater. Chem. A*, 2015, **3**, 9707-9713.
30. A. Zhao, J. Masa, W. Xia, A. Maljusch, M.-G. Willinger, G. Clavel, K. Xie, R. Schlögl, W. Schuhmann and M. Muhler, *J. Am. Chem. Soc.*, 2014, **136**, 7551-7554.
31. D. J. Li, U. N. Maiti, J. Lim, D. S. Choi, W. J. Lee, Y. Oh, G. Y. Lee and S. O. Kim, *Nano Lett.*, 2014, **14**, 1228-1233.
32. F. Lai, Y.-E. Miao, Y. Huang, Y. Zhang and T. Liu, *ACS Appl. Mater. Interfaces*, 2015, **7**, DOI: 10.1021/acsami.1025b06274.
33. G. Dong, M. Fang, H. Wang, S. Yip, H.-Y. Cheung, F. Wang, C.-Y. Wong, S. T. Chu and J. C. Ho, *J. Mater. Chem. A*, 2015, **3**, 13080-13086.
34. H.-W. Liang, S. Bruller, R. Dong, J. Zhang, X. Feng and K. Mullen, *Nat. Coummun.*, 2015, **6**, 7992.
35. H. Zhang, Z. Ma, J. Duan, H. Liu, G. Liu, T. Wang, K. Chang, M. Li, L. Shi, X. Meng, K. Wu and J. Ye, *ACS Nano*, 2015, **9**, DOI: 10.1021/acsnano.1025b05728.
36. M. S. Thorum, J. M. Hankett and A. A. Gewirth, *J. Phys. Chem. Lett.*, 2011, **2**, 295-298.
37. R. A. Rincón, J. Masa, S. Mehrpour, F. Tietz and W. Schuhmann, *Chem. Commun.*, 2014, **50**, 14760-14762.
38. H. Zhang, Y. Li, G. Zhang, T. Xu, P. Wan and X. Sun, *J. Mater. Chem. A*, 2015, **3**, 6306-6310.
39. H. Zhang, B. Yang, X. Wu, Z. Li, L. Lei and X. Zhang, *ACS Appl. Mater. Interfaces*, 2015, **7**, 1772-1779.
40. X. Yan, L. Tian, M. He and X. Chen, *Nano Lett.*, 2015, **15**, 6015-6021.

View Article Online
DOI: 10.1039/C6TA00223D



# Graphical Abstract

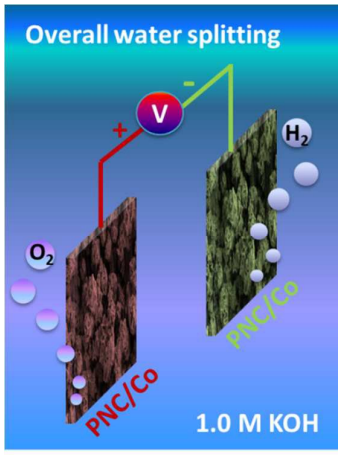


Cobalt nanoparticles embedded in porous N-rich carbon (PNC/Co) can perform as both the active cathode and anode materials to drive the overall water splitting in alkaline media for simultaneous electro-generation of hydrogen and oxygen gases.